Article type: Original

Aluminum Nanotripods for Light-Matter Coupling Robust to Nanoemitter Orientation

Víctor Pacheco-Peña[1,2], Antonio I. Fernández-Domínguez[3], Yu Luo[4], Miguel Beruete[1,5] and Miguel Navarro-Cía[6,]*

*Corresponding Author: E-mail: m.navarro-cia@bham.ac.uk

[1]Antennas Group−TERALAB, Universidad Pública de Navarra, Pamplona 31006, Spain
[2]Department of Electrical and Systems Engineering, University of Pennsylvania, Philadelphia, PA 19104, USA
[3]Departamento de Física Teórica de la Materia Condensada and Condensed Matter Physics Center (IFIMAC), Universidad Autónoma de Madrid, Madrid 28049, Spain
[4]School of Electrical & Electronic Engineering, Nanyang Technological University, Singapore 639798, Singapore
[5]Institute of Smart Cities, Universidad Pública de Navarra, Pamplona 31006, Spain
[6]School of Physics and Astronomy, University of Birmingham, Birmingham B15 2TT, U.K.

Nanoantennas enable the concentration and manipulation of light at the (sub-)nanoscale. This ability offers novel strategies to strengthen light-matter interactions in a controlled fashion. However, most nanoantennas are highly sensitive to light polarization and emitter orientation, which is disadvantageous for many applications (e.g., Raman and fluorescence spectroscopy depend strongly on molecular symmetry and orientation, as well as on the local optical field gradient). It is also unfortunate that analytical descriptions, essential to bridge experimental observations to knowledge and future design guidelines, have lagged behind. Here, resorting to conformal transformation, aluminum nanotripods excited by a nanoemitter of arbitrary orientation are studied analytically. Our results, corroborated with full-wave simulations, show that aluminum nanotripods are robust not only to emitter orientation, but also to its position. Hence, this work exemplifies the effectiveness and efficiency of transformation optics to analytically describe and optimize light-matter interaction in complex plasmonic nanoantennas.

1. Introduction

The rapidly expanding field of nanoantennas has opened up new ways to manipulate light and light-matter interactions at the nanometric scale with unprecedented precision and efficiency. This new technology has already shown profound implications in areas as varied as photocatalysis,[1] photovoltaics,[2] and light-emitting [3] and spectroscopy applications.[4] Gap nanoantennas, and more specifically dimers [5–10] and particle on a mirror [11–16] geometries, have become archetypal designs of optical nanocavities for light-matter coupling. In recent years, much research attention has focused on exploiting these plasmonic devices to overcome the 3 orders of magnitude spatial mismatch between typical optical wavelengths (~1 μm) and nanoemitter (dye molecule and quantum dots) sizes (~1 nm). This is possible thanks to the large electromagnetic (EM) field concentration and enhancement enabled by localized surface plasmons (LSPs) supported by metallic nanostructures at optical frequencies.

The evanescently confined nature of LSPs is a direct consequence of the vector nature of light, which makes these EM modes strongly sensitive to polarization. Thus, the efficiency in the far- and near-field excitation of LSPs depends strongly on the orientation of the incident fields (propagating radiation and point dipole sources, respectively). This dependence represents an important limitation, which is hindering the application of gap antennas [5-16] as plasmonic cavities (where the gap axis defines a preferential direction). Note that standard fabrication and deposition techniques do not allow for the control of the orientation of (single or collective) nanoemitters, and so, nanoemitters are randomly oriented in most experiments. A way to circumvent the polarization-dependence constraint consists in using C_3 rotational symmetry antennas [17–20] (typically composed of three triangular-shaped particles arranged in a tripod-like fashion). This antenna geometry has proven to be virtually polarization-independent under out-of-plane far-field illumination.[21]

Here, we investigate the transfer of the far-field polarization-robustness of nanotripods to its near-field excitation; an attribute which would make this antenna geometry an ideal candidate for light-matter coupling applications. With this purpose, we develop a theoretical approach for the description of the Purcell enhancement experienced by an emitter placed in the vicinity of plasmonic tripods. We use this physical magnitude for the assessment of the performance of these devices as open nanocavities. Our method is based on transformation optics (TO) ideas,[22–24] and in order to keep the analytical character of our results, we restrict it to two-dimensional (2D) nanotripods and dipole sources (translationally invariant along the out-of-plane direction). Despite limiting severely its quantitative prediction capabilities for real three-dimensional (3D) scenarios, the 2D nature of our treatment provides a deep physical insight into the key factors that govern the EM properties of the system and the 3D counterpart. Similar strategies have proven to be very successful in the case of crescent-shaped and dimer antennas.[25–27] More recently, TO-based approaches have also been extended to the description of weak [28] and strong coupling phenomena.[29]

2. Analytical framework

As discussed above, the simplest nanoantenna with C_3 rotational symmetry is a nanotripod, see **Figure 1**. This morphology is very attractive because it can be fabricated in any size via inexpensive colloidal processing techniques enabling the shift of its LSP resonances to any spectral range.[30] We consider a realistic two-dimensional 8 nm-pod-length aluminum (Al) tripod whose LSP resonances are expected to lie in the visible and ultraviolet.[31,32] The three nanopods are connected smoothly using Bézier poligons that start at 0.5 nm from the nanotripod center; L_1' and L_2' represent the distance from the nanoantenna radius (8 nm) and the connecting tapers (0.5 nm) to the circumference of radius 1 nm, respectively. The deeply sub-wavelength dimensions of this structure ($< \lambda_0/12$ for the spectral window of interest, 200 nm $< \lambda_0 <$ 1000 nm) allows its quasi-static treatment. Thus, the electric field is fully described

3

by an electrostatic potential satisfying Laplace's equation, which makes it possible to describe fully analytically the response of the nanotripod excited by a randomly oriented dipole under the conformal transformation framework.[33] Importantly, this endows a complete physical understanding of this scenario and other C_3 rotational symmetry nanoantennas.

By applying the conformal transformation $z = \ln(z'/a)$ [34,35] (where $z = x + iy$ and $z' = x' + iy'$ are the spatial coordinates in the transformed and original frame, respectively; and a denotes the distance between the emitter and the coordinate origin), the nanotripod with out-of-plane translation symmetry and the line dipole source with random orientation are transformed into an infinitely periodic comb geometry and an array of line dipoles located every three teeth. The unit cell comprising three teeth and a line dipole has periodicity 2π along y-direction. Analytical solutions to Laplace's equation in this transformed frame can be obtained using the methodology detailed in the Supporting Information.

The main consequence of the quasi-static treatment and the 2D conformal analysis is that the power dissipation in the original, $P_{abs}^{(x',y')}$, and transformed, $P_{abs}^{(x,y)}$, frames are identical. The latter can be computed straightforwardly by evaluating the electric field at the dipole position, as follows:

$$P_{nr} = P_{abs}^{(x',y')} = P_{abs}^{(x,y)} = -\frac{1}{2}\omega \operatorname{Im}\left\{\overline{p}^* \cdot \overline{E}_1^s(x,y)\right\} = -\frac{1}{2}\omega \operatorname{Im}\left\{p_x E_{1x}^s(x,y) + p_y E_{1y}^s(x,y)\right\} \tag{1}$$

where P_{nr} denotes the nonradiative power emission by the dipole source, $\omega = 2\pi c/\lambda_0$ is the angular frequency at the working wavelength λ_0 and c is the velocity of light in vacuum. The components of the emitter dipole moment along the x and y directions are p_x and p_y, and E_{1x}^s

4

and E_{1y}^s are the electric field amplitudes at the emitter position ($-L_2 < x < L_1$ and $-d_2 < y < d_1$).

Notice that the nanoemitter intrinsic quantum yield is set to 1 in the calculations in order to correlate the nonradiative decay experienced by the nanoemitter with the power absorbed by the nanotripod.[36] Hence, the nonradiative Purcell enhancement rate spectra is given by $\overline{\Gamma_{nr}} = P_{nr}(\omega)/P_0(\omega)$, where P_0 is the power radiated by the dipole in free space, calculated as $P_0 = (1/16)(\omega^3 \mu_0)|p|^2$ with μ_0 the permeability of vacuum and $|p|$ the magnitude of the dipole moment.

3. Computational methods

The commercial finite element analysis software Comsol Multiphysics® is used to validate the analytical results. The metal (Al) permittivity is modeled using an analytical polynomial equation. This function fits Palik's experimental data (see the Supplementary Information for further details).[37] The nanotripods (with total diameter of 16 nm) are embedded in vacuum, modeled as a two-dimensional square 700 nm × 700 nm box enclosed by scattering boundary conditions (i.e., perfectly matched layers). The nanoemitter is modeled using two anti-parallel in-plane magnetic currents with a separation of 5 pm. A fine mesh is used with a maximum and minimum element size of 5 nm and 10 pm, respectively, within the vacuum region. A refined mesh, twice smaller than in vacuum, is used within the nanotripods to ensure accurate results.

4. Results

4.1. The effect of the flare angle θ'

From the divergence condition for the expansion coefficients of the scattered quasi-static potential, the spectral position of the LSP modes is readily available as a function, for instance, of the flare angle θ' – i.e., the angular pod thickness θ' – (see **Figure 2a,b**). One can notice the large accumulation of higher order LSPs in the ultraviolet range, close to the surface

5

plasmon wavelength (λ_{sp}), whereas the fundamental dipole-active LSP emerges within the visible spectrum. As θ' increases, the spectral position of higher order LSPs does not change significantly. However, the fundamental LSP experiences a large blue-shift from orange ($\theta' = 10°$) to violet ($\theta' = 45°$), it then red-shifts into the blue spectral band for $\theta' > 90°$ (note the non-monotonic behavior in Figure 2a,b).

The LSP resonance phenomenology discussed above manifests clearly in the analytical $\overline{\Gamma_{nr}}$-map for a nanotripod excited by a vertically or horizontally oriented dipole at $(x', y') = (1\ nm, 0)$ – which is the middle point between two pods –; see **Figure 2c,d**, respectively. As a result of the C_3 rotational symmetry (and the semitransparency of the thin Al pods in the visible and ultraviolet), the LSPs of the nanotripod are excited regardless of the dipole orientation. The maximum $\overline{\Gamma_{nr}}$ (associated to the fundamental LSP) emerges around 660 nm for $\theta' = 10°$, is blue-shifted up to 413 nm for $\theta' = 45°$ and undergoes a red-shift up to 444 nm for $\theta' = 90°$. Remarkably, this trend holds for both dipole orientations, despite the fact the fundamental LSP modes excited under these two orientations are inherently different, as shown in **Figure 2g,h**. Higher order LSPs experience also a similar θ'-drift, but less prominent than the dipole one.

In contrast to the spectral position of the $\overline{\Gamma_{nr}}$ maxima, the emitter-LSP coupling strength (i.e., the $\overline{\Gamma_{nr}}$ magnitude at resonance) depends indeed on the orientation of the dipole. Hence, non-radiative Purcell enhancement has different values for each dipole orientation. Namely, for the vertical dipole, $\overline{\Gamma_{nr}}$ is approximately ten times larger than that for the horizontal dipole when evaluated at the fundamental LSP resonance. In contrast, this difference is only a factor of 2 at the peak associated to the second LSP supported by the nanotripod.

As a validation of our analytical approach, $\overline{\Gamma_{nr}}$ spectra computed via full-wave electrodynamic simulations are displayed in **Figure 2e,f**. The simulated Purcell enhancement maps are in very good agreement with the analytical $\overline{\Gamma_{nr}}$. Numerical calculations of the radiative Purcell enhancement spectra $\overline{\Gamma_r}$ (calculated as the power radiated by the nanotripod under the dipole illumination, P_r, normalized to P_0) and the absorption cross section confirms the negligible radiation losses experienced by the system (see **Figure S4**), which justifies the analytical methodology followed here. From now on, we focus on the analytical results of the nanotripod with $\theta' = 10°$ which is the most robust design in terms of $\overline{\Gamma_{nr}}$ peak wavelength and magnitude against dipole orientation (among the range of pod angles considered).

4.2. The effect of the emitter and nanotripod orientation

The dependence of the emitter-LSP coupling strength with the source orientation can be tracked in **Figure 3a**. It shows that $\overline{\Gamma_{nr}}$ at the fundamental LSP drops by a factor of ~1.6 from vertical ($\overline{\Gamma_{nr}} = 2.3 \times 10^4$) to 45° dipole orientation, and an additional ~6.3 factor from 45° to horizontal dipole orientation ($\overline{\Gamma_{nr}} = 2.3 \times 10^3$). Similar calculations for the fundamental LSP sustained by an Al nanobipod (i.e., nanodiabolo [38]) yield a $\overline{\Gamma_{nr}}$ decay of ~1.5 from vertical ($\overline{\Gamma_{nr}} = 7.5 \times 10^3$) to 45° orientation, and an additional ~9 from 45° to horizontal orientation ($\overline{\Gamma_{nr}} = 613$). This comparison exemplifies the convenience of using nanotripods for light-matter coupling at the nanoscale, exploiting their little sensitivity to the nanoemitter orientation (in comparison to monopods and bipods).

For comparison purposes, the numerical $\overline{\Gamma_{nr}}$ and $\overline{\Gamma_r}$ corresponding to this scenario are given in the Supporting Information (**Figure S5**), together with complementary results for an example of the more dipole-orientation-sensitive design $\theta' = 25°$ (**Figure S6**). In those results

it is evident that $\overline{\Gamma_{nr}}$ and $\overline{\Gamma_r}$ display similar dependence to the dipole orientation. This locking between $\overline{\Gamma_{nr}}$ and $\overline{\Gamma_r}$ comes from the fact that both enhancements are governed by the same LSP modes.

In a real scenario, the position of the nanoemitter between two pods of the nanoantenna cannot be determined with high precision. To investigate this situation, **Figure 3b,c,d** show $\overline{\Gamma_{nr}}$ for vertical, 45° and horizontal orientations as the nanotripod is rotated an angle ξ (see insets to better appreciate the rotation angle). $\overline{\Gamma_r}$ can be found in **Figure S7**, together with the complementary analytical and numerical results for $\theta' = 25°$ (**Figure S8**). Effectively, this rotation is equivalent to displacing the emitter along a circumference arc of radius 1 nm. The dependence of $\overline{\Gamma_{nr}}$ (i.e., light-matter coupling strength) on ξ is noticeable for the three dipole orientations ψ = 0° (vertical), 45° and 90° (horizontal). The maximum variation of $\overline{\Gamma_{nr}}$ in the worst case scenario (corresponding to ψ = 90°) is a factor of 10.7, from 2.42×10^3 for ξ = 0° to 2.58×10^4 for ξ = ±30°.

4.3. The effect of the emitter position
The impact of displacing the nanoemitter along x' on $\overline{\Gamma_{nr}}$ is depicted in **Figure 4a,b**, whereas the negligible $\overline{\Gamma_r}$ can be found in **Figure S9**. For large emitter-tripod core distances, $\overline{\Gamma_{nr}}$ is low for all LSP modes. As the dipole source approaches the nanotripod core, $\overline{\Gamma_{nr}}$ rises gradually, indicating that the emitter-LSP coupling strengthens. The enhancement in the light-matter interaction originates from the excitation of higher order LSPs; the closer the nanoemitter is to the nanostructure surface, the more efficiently it couples to higher order LSPs.[16,19,29] This holds true for any nanotripod geometry as the results for $\theta' = 25°$ demonstrates in **Figure S10**. In order to show this effect more clearly, $\overline{\Gamma_{nr}}$ versus wavelength

8

for two different dipole locations, $x' = 0.75$ nm and $x' = 6$ nm, is plotted in **Figure 4c** (vertical orientation) and **4d** (horizontal orientation) along with the simulation results (empty dots). Good quantitative agreement between analytical and simulation results is observed. These two panels illustrate the influence of the emitter position and orientation on $\overline{\Gamma_{nr}}$. Note that for each x'-position, $\overline{\Gamma_{nr}}$ will undergo the same trend with varying ξ as shown in Figure 3. For completeness, the field distribution evaluated at the various Purcell enhancement maxima for $x' = 0.75$ is shown in the Supplementary Information.

5. Conclusion

To conclude, the performance aluminum nanotripods with C_3 rotational symmetry for light-matter coupling applications has been thoroughly investigated. Their excitation by a point dipole source modelling a nanoemitter with arbitrary orientation has been studied analytically using a conformal transformation approach. Our analytical results reveal that these nanostructures are remarkably robust against emitter position and orientation, demonstrating an excellent agreement with numerical calculations. Our findings prove that nanotripods are excellent candidates for nanocavity applications involving large ensembles of emitters, whose position and orientation are inherently random. The electrostatic approximation used here could be extended to deal with larger radiative nanoantennas using energy arguments rather than considering the magnetic field so that the analytical character is retained.[22, 33, 39] Extending the analytical frame to 3D scenarios may be possible, but the results would not be completely analytical.[23, 27, 29]

Supporting Information

Additional supporting information may be found in the online version of this article at the publisher's website.

Figure S1: Sketch of the transformed scenario, an Al comb, along with the relevant coefficients and geometrical parameters.

Figure S2: Aluminum complex permittivity used throughout this manuscript.

Figure S3: Number of modes as a function of θ' when a vertical (blue) and a horizontal (red) oriented dipole illuminates the nanotripod.

Figure S4: Analytical (a, b) and numerical (c, d) nonradiative Purcell enhancement, along with the numerical radiative Purcell spectra (e, f) and absorption cross section (g, h), for 8 nm long arm tripods with varying θ' under vertical (first column) and horizontal dipole (second column) excitation [plane-wave excitation for (g, h)]. The contourplots in panels a-f are in logarithmic color scale. On the contrary, the contour plots in panels g and h are in linear scale to better appreciate the results.

Figure S5: Analytical (a) and simulation (b) results of the nonradiative Purcell enhancement along with the radiative spectra (c) for an Al nanotripod with $\theta' = 10^o$ illuminated by a dipole source with different orientations ranging from 0 to 90°. The contour plots are in linear scale to better appreciate the results.

Figure S6: Analytical (a) and simulation (b) results of the nonradiative Purcell enhancement along with the radiative spectra (c) for an Al nanotripod with $\theta' = 25^o$ illuminated by a dipole source with different orientations ranging from 0 to 90°. The contour plots are in linear scale to better appreciate the results.

Figure S7: Analytical (first row) and numerical (second row) results of the nonradiative Purcell enhancement, along with the radiative spectra (third row) for a nanotripod with $\theta' = 10^o$ (and touching arms), when it is rotated from -30° to 30°. The tripods are excited by a point dipole with orientation: vertical (first column), 45° (second column), and horizontal (third column). The contour plots are in linear scale to better appreciate the results.

Figure S8: Analytical (first row) and numerical (second row) results of the nonradiative Purcell enhancement, along with the radiative spectra (third row) for a nanotripod with $\theta' = 25^o$, when it is rotated from -30° to 30°. The tripods are excited by a point dipole with orientation: vertical (first column), 45° (second column), and horizontal (third column). The contour plots are in linear scale to better appreciate the results.

Figure S9: Simulation results of the nonradiative Purcell enhancement (first row) along with the radiative spectra (third row) for a nanotripod with $\theta' = 10^o$. The dipole source is displaced along the x' axis from 0.5 to 8 nm for different emitter orientations: vertical (first column), horizontal (second column). The contour plots are in linear scale to better appreciate the results. The panels in the second row show the nonradiative Purcell enhancement extracted from panels (a, b) for $x' = 0.75$ nm and $x' = 6$ nm for vertical (c) and horizontal (d) orientation.

Figure S10: Simulation results of the nonradiative Purcell enhancement (first row) along with the radiative Purcell spectra (third row) for a nanotripod with $\theta' = 25^{\circ}$. The dipole source is displaced along the x' axis from 0.5 to 8 nm for different emitter orientations: vertical (first column), horizontal (second column). The contour plots are in linear scale to better appreciate the results. The panels in the second row show the nonradiative Purcell enhancement extracted from panels (a, b) for $x' = 0.75$ nm and $x' = 6$ nm for vertical (c) and horizontal (d) orientation.

Figure S11: Phase correction $\Delta\varphi_1$ (first column) and $\Delta\varphi_2$ (second column) as a function of θ' when a vertical (first row) and horizontal (second row) dipole is used.

Figure S12: Snapshot of the $E'_{\varphi'}$ field for a tripod nanoantenna with $\theta' = 10^{\circ}$ excited with a vertically oriented dipole placed at $x' = 0.75$ nm. The field distributions are evaluated at the nonradiative Purcell enhancement peaks found in Fig. S9c. The inset of each panel shows a zoom-in of the field distribution at the center of the nanotripod. Note that the color scale has been saturated from -0.1 to 0.1 in order to better appreciate the field distribution.

Figure S13: Snapshot of the $E'_{\varphi'}$ field for a tripod nanoantenna with $\theta' = 25^{\circ}$ excited with a vertically oriented dipole placed at $x' = 0.75$ nm. The field distributions are evaluated at the nonradiative Purcell enhancement peaks found in Fig. S10c. The inset of each panel shows a zoom-in of the field distribution at the center of the nanotripod. Note that the color scale has been saturated from -0.1 to 0.1 in order to better appreciate the field distribution.

Figure S14: Snapshot of the $E'_{\rho'}$ field for a tripod nanoantenna with $\theta' = 25^{\circ}$ excited with a horizontally oriented dipole placed at $x' = 0.75$ nm. The field distributions are evaluated at the nonradiative Purcell enhancement peaks in Fig. S10d. The inset of each panel shows a zoom-in of the field distribution at the center of the nanotripod. Note that the color scale has been saturated from -0.1 to 0.1 in order to better appreciate the field distribution.

Figure S15: Snapshot of the $E'_{\rho'}$ field for a tripod nanoantenna with $\theta' = 25^{\circ}$ excited with a horizontally oriented dipole placed at $x' = 0.75$ nm. The field distributions are evaluated at the nonradiative Purcell enhancement peaks in Fig. S10d. The inset of each panel shows a zoom-in of the field distribution at the center of the nanotripod. Note that the color scale has been saturated from -0.1 to 0.1 in order to better appreciate the field distribution.

## References

[1]   M. Salmistraro, A. Schwartzberg, W. Bao, L. E. Depero, A. Weber-Bargioni, S. Cabrini, I. Alessandri, *Small* **9**, 3301–3307 (2013).

[2]   H. A. Atwater, A. Polman, *Nat. Mater.* **9**, 205–213 (2010).

[3]   J.-J. Greffet, *Science* **308**, 1561-1563 (2005).

[4]   V. Giannini, A. I. Fernández-Domínguez, S. C. Heck, S. A. Maier, *Chem. Rev.* **111**, 3888–3912 (2011).

[5]   A. Kinkhabwala, Z. Yu, S. Fan, Y. Avlasevich, K. Müllen, W. E. Moerner, *Nat. Photonics* **3**, 654–657 (2009).

[6]   M. Righini, P. Ghenuche, S. Cherukulappurath, V. Myroshnychenko, F. J. García de Abajo, R. Quidant, *Nano Lett.* **9**, 3387–3391 (2009).

[7]   H. Aouani, M. Rahmani, M. Navarro-Cía, S. A. Maier, *Nat. Nanotechnol.* **9**, 290–294 (2014).

[8]   T. Shoji, Y. Tsuboi, *J. Phys. Chem. Lett.* **5**, 2957–2967 (2014).

[9]   A. Varas, P. García-González, F. J. García-Vidal, A. Rubio, *J. Phys. Chem. Lett.* **6**, 1891–1898 (2015).

[10]   K. Santhosh, O. Bitton, L. Chuntonov, G. Haran, *Nat. Commun.* **7**, 11823 (2016).

[11]   C. Ciracì, R. T. Hill, J. J.; Mock, Y. Urzhumov, A. I. Fernández-Domínguez, S. A. Maier, J. B. Pendry, A. Chilkoti, D. R. Smith, *Science* **337**, 1072–1075 (2012).

[12]   G. M. Akselrod, C. Argyropoulos, T. B. Hoang, C. Ciracì, C. Fang, J. Huang, D. R. Smith, M. H. Mikkelsen, *Nat. Photonics* **8**, 835–840 (2014).

[13]   D. O. Sigle, L. Zhang, S. Ithurria, B. Dubertret, J. J. Baumberg, *J. Phys. Chem. Lett.* **6**, 1099–1103 (2015).

[14]   G. Zengin, M. Wersäll, S. Nilsson, T. J. Antosiewicz, M. Käll, T. Shegai, *Phys. Rev. Lett.* **114**, 157401 (2015).

[15]   A. Lombardi, A. Demetriadou, L. Weller, P. Andrae, F. Benz, R. Chikkaraddy, J. Aizpurua, J. J. Baumberg, *ACS Photonics* **3**, 471–477 (2016).

[16]   R. Chikkaraddy, B. de Nijs, F. Benz, S. J. Barrow, O. A. Scherman, E. Rosta, A. Demetriadou, P. Fox, O. Hess, J. J. Baumberg, *Nature* **535**, 1–4 (2016).

[17]   T. Shegai, Z. Li, T. Dadosh, Z. Zhang, H. Xu, G. Haran, *Proc. Natl. Acad. Sci. U. S. A.* **105**, 16448–16453 (2008).

[18]   L. Chuntonov, G. Haran, *Nano Lett.* **11**, 2440–2445 (2011).

[19]   A. L. Koh, A. I. Fernández-Domínguez, D. W. McComb, S. A. Maier, J. K. W. Yang, *Nano Lett.* **11**, 1323–1330 (2011).

[20]   S. J. Barrow, S. M. Collins, D. Rossouw, A. M. Funston, G. A. Botton, P. A. Midgley, P. Mulvaney, *ACS Nano* **10**, 8552–8563 (2016).

[21]   H. Aouani, M. Navarro-Cía, M. Rahmani, T. P. H. Sidiropoulos, M. Hong, R. F. Oulton, S. A. Maier, *Nano Lett.* **12**, 4997–5002 (2012).

[22]   J. B. Pendry, A. Aubry, D. R. Smith, S. A. Maier, *Science* **337**, 549–552 (2012).

[23] J. B. Pendry, A. I. Fernández-Domínguez, Y. Luo, R. Zhao, *Nat. Phys.* **9**, 518–522 (2013).

[24] J. B. Pendry, Y. Luo, R. Zhao, *Science* **348**, 521–524 (2015).

[25] A. Aubry, D. Y. Lei, S. A. Maier, J. B. Pendry, *Phys. Rev. Lett.* **105**, 233901 (2010).

[26] Y. Luo, D. Y. Lei, S. A. Maier, J. B. Pendry, *Phys. Rev. Lett.* **108**, 023901 (2012).

[27] Y. Luo, R. Zhao, A. I. Fernández-Domínguez, S. A. Maier, J. B. Pendry, *Sci. China Inf. Sci.* **56**, 1–13 (2013).

[28] V. Pacheco-Peña, M. Beruete, A. I. Fernández-Domínguez, Y. Luo, M. Navarro-Cía, *ACS Photonics* **3**, 1223-1232 (2016).

[29] R.-Q. Li, D. Hernangómez-Pérez, F. J. García-Vidal, A. I. Fernández-Domínguez, *Phys. Rev. Lett.* **117**, 107401 (2016).

[30] S. Chen, Z. L. Wang, J. Ballato, S. H. Foulger, D. L. Carroll, *J. Am. Chem. Soc.* **125**, 16186–16187 (2003).

[31] J. M. Sanz, D. Ortiz, R. Alcaraz de La Osa, J. M. Saiz, F. González, A. S. Brown, M. Losurdo, H. O. Everitt, F. Moreno, *J. Phys. Chem. C* **117**, 19606–19615 (2013).

[32] A. M. Watson, X. Zhang, R. Alcaraz de la Osa, J. M. Sanz, F. González, F. Moreno, G. Finkelstein, J. Liu, H. O. Everitt, *Nano Lett.* **15**, 1095-1100 (2015).

[33] A. V. Zayats, S. A. Maier, *Active Plasmonics and Tunable Plasmonic Metamaterials* (John Wiley & Sons, Hoboken, NJ, 2013); pp. 105–152.

[34] M. Navarro-Cía, S. A. Maier, *ACS Nano* **6**, 3537–3544 (2012).

[35] Y. Luo, J. B. Pendry, A. Aubry, *Nano Lett.* **10**, 4186–4191 (2010).

[36] L. Novotny, B. Hecht, *Principles of Nano-Optics* (Cambridge University Press, U.K., 2012).

[37] E. D. Palik, *Handbook of Optical Constants of Solids* (Academic, 1985).

[38] Z. J. Coppens, W. Li, D. G. Walter, J. G. Valentine, *Nano Lett.* **13**, 1023-1028 (2013).

[39]   M. Kraft, Y. Luo, J. B. Pendry, *Nano Lett.* **16**, 5156-5162 (2016).
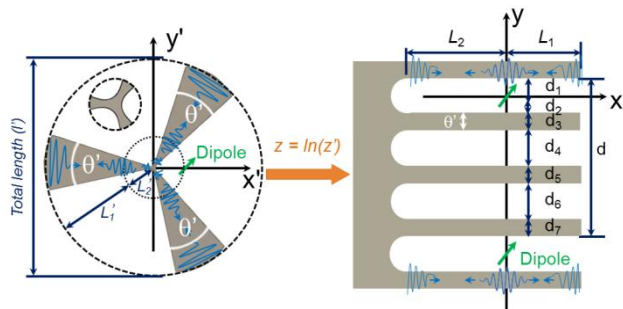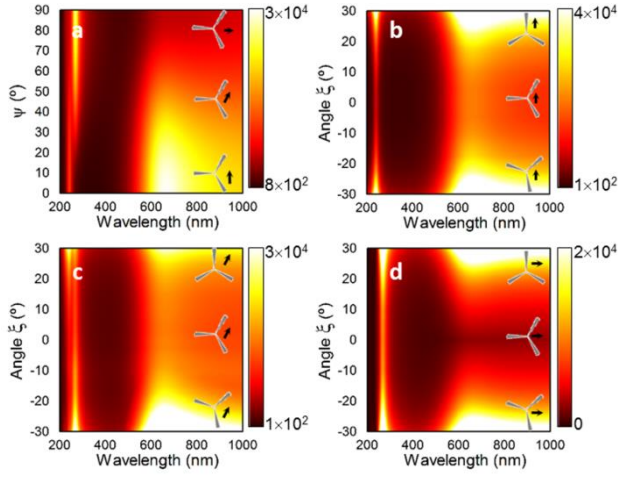
Figure 1. Al nanotripod excited by a nanoemitter, along with its transformed counterpart, an Al comb, obtained after applying the conformal mapping indicated in the figure.
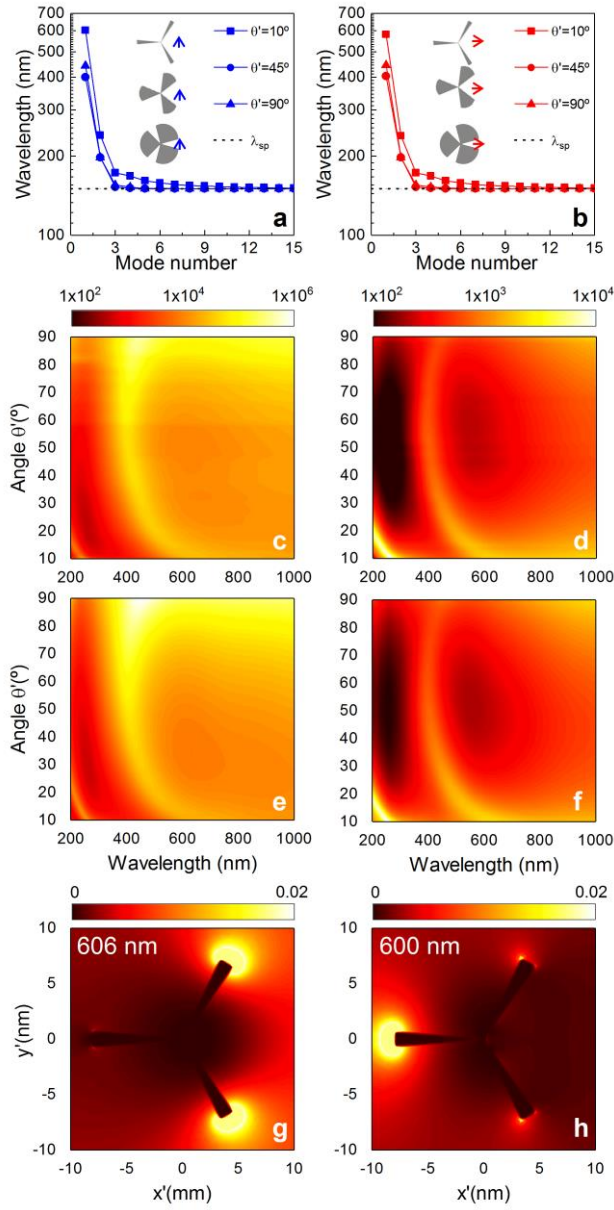
Figure 2. Analytical resonant wavelength for the LSP modes supported by nanotripods with angle $\theta' = 10°$ (squares), $45°$ (circles) and $90°$ (triangles), excited under vertical (a) and horizontal (b) dipole orientation, as shown in the insets. Note that the discrete points have been connected with solid lines to guide the eye. The λ_{sp} of the metal (Al) is shown as dashed line. Analytical (c, d) and numerical (e, f) $\overline{\Gamma_{nr}}$ for 8 nm long arm tripods with varying θ' under vertical (first column) and horizontal dipole (second column) excitation. The contour plots are in logarithmic color scale. Numerical electric field intensity distribution $|E(x', y')|^2$ of the fundamental LSP mode for $\theta' = 10°$ under vertical (g) and horizontal (h) dipole excitation.

Figure 3. (a) Analytical $\overline{\Gamma_{nr}}$ for a nanotripod with $\theta' = 10°$ excited by an emitter at (1 nm, 0) and with different orientations, ranging from 0° (vertical) to 90° (horizontal). (b,c,d) Analytical $\overline{\Gamma_{nr}}$ for a nanotripod with $\theta' = 10°$ as a function of the rotation angle ξ (between -30° and 30°) under vertical (b), 45° (c) and horizontal (d) dipole excitation. Note the linear color scale in all the contour plots.
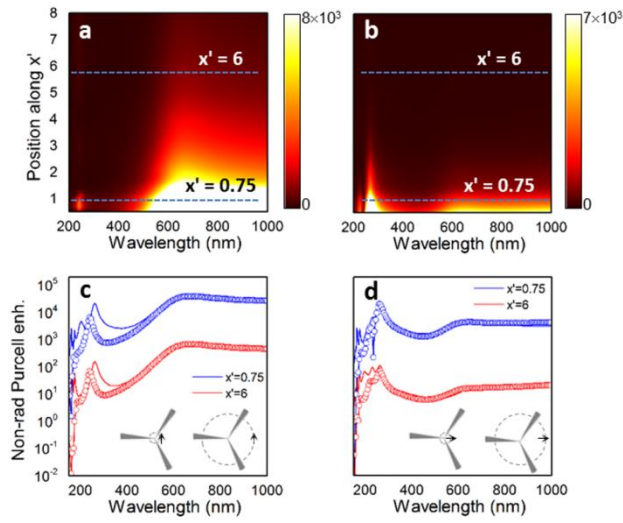
Figure 4. Analytical $\overline{\Gamma_{nr}}$ for a $\theta' = 10°$ nanotripod versus emitter position along x'-axis from 0.5 to 8 nm: vertical (a) and horizontal (b) orientation. The color maps are in linear scale. $\overline{\Gamma_{nr}}$ spectra for dipoles at $x' = 0.75$ nm and $x' = 6$ nm under vertical (c) and horizontal (d) orientation: analytical (solid lines) and numerical spectra (empty dots). These plots have been extracted from panels (a) and (b), as shown by blue dashed lines.

Graphical Abstract

Nanoantennas are a thriving research field, which is creating transformative opportunities for controlling light-matter interaction at the (sub-)nanoscale. Experiments involving nanoemitters and nanoantennas are nowadays routinely measured in the lab. However, interpretation of the observations is not always straightforward. Conformal transformation is used here to provide an analytical description of nanotripods coupled to nanoemitters and to unveil those designs robust to the relative orientation between the nanoemitter and the nanotripod.

ToC figure